



Design optimization of a three-dimensional diffusing S-duct using a modified SST turbulent model



Wenbiao Gan^{a,*}, Xiaocui Zhang^b

^a Beijing University of Aeronautics and Astronautics, Beijing, 100191, People's Republic of China

^b The First Aircraft Design Institute of Aviation Industry Corporation of China, Xi'an, 710089, People's Republic of China

ARTICLE INFO

Article history:

Received 20 June 2016

Received in revised form 19 December 2016

Accepted 22 December 2016

Available online 28 December 2016

Keywords:

S-duct

Design optimization

Modified SST turbulent model

Separation

Flow distortion

Total pressure recovery

ABSTRACT

This paper examines design optimization of a three-dimensional diffusing S-duct using a modified $k-\omega$ shear stress transport (SST) turbulent model as a turbulence prediction method. According to based-Reynolds-stress and based-separation ideas, a robust solution procedure for the model is described and a grid convergence study is presented. An automated system employs this model to design an S-duct. The aerodynamic performances of the optimal duct are investigated in on-design and off-design conditions. It is shown that the sensitivity of the modified model with respect to shape variations allows its use in the design system. Using a multi-objective optimization strategy, this design system significantly improves aerodynamic performance of the S-duct and has low computation cost and excellent design efficiency. The centerline's curvature and the cross-sectional area ratio become reasonable to avoid overexpansion of the optimal duct. Compared with the original design, the flow distortion coefficient of the optimal duct is reduced by 16.3% and the total pressure recovery factor is increased by 1.1% in on-design condition.

© 2016 Elsevier Masson SAS. All rights reserved.

1. Introduction

Modern advance aircraft should have high stealth performance. To reduce radar cross section (RCS) of propulsion system, typical advance stealth aircraft (such as the RQ180) always employs an S-duct. This duct has complex shape and special aerodynamic performance, which is mainly affected by two factors: 1) the flow distortion, 2) the total pressure recovery.

The flow distortion will produce cross flow pressure gradient and induce a secondary flow. At the same time, the boundary layer and the secondary flow will interfere with each other and cause detached vortex. These may lead to more serious total pressure loss and flow distortion.

Many scholars had done lots of researches to improve aerodynamic performance of the S-duct. Faced by total pressure loss and velocity distribution, Weske [1] carried out the experiment of an S-duct. Guo [2] investigated swirl in the S-duct. It was shown that at high incidence there was flow separation after the first bend and a pair of contra-rotating vortices in the flow after the second bend. These features caused serious flow distortion of the S-duct. The experimental flow distortion of the S-duct was analyzed by Seddon [3]. To improve aerodynamic performance of the S-duct,

practical intake aerodynamic design was introduced by Goldsmith [4] and indicated the computational fluid dynamics (CFD) was promising for intake design. Numerical simulation of the S-duct has been developing rapidly in recent years. Xiao [5] applied a modified $k-\omega$ turbulence model to investigate transonic flow features of an S-duct. Based on RNG $k-\varepsilon$ turbulence model, Saha [6] studied flow characteristics of the S-duct. Gerolymos [7] adopted Reynolds stress model to analyze the flowfield structure of a dual S-duct. Zhang [8] used $k-\varepsilon$ turbulence model to design an S-duct. The sensitivity of different turbulence models was investigated for the S-duct by Lee [9]. It indicated that the result of Menter's $k-\omega$ Shear Stress transport (SST [10]) model was more reliable than the other three models. Zhang [11] investigated multidisciplinary design strategy of an S-duct, which used SST $k-\omega$ turbulence model for numerical simulation. Aranake [12] employed MOGA-II and SST $k-\omega$ turbulence model to design a low-speed S-duct. Using the basic SST $k-\omega$ turbulence model as a turbulence prediction method, Magnus [13] and Paul [14] analyzed the S-duct with vortex generators. These studies mostly focused on flow analysis and controlling swirl of the S-duct, but didn't pay special attention to conformal stealth constraint of the airframe. Though the controlling swirl can improve aerodynamic performance, sometimes it has difficulty with automatic realization of optimization. Therefore, it is necessary to consider conformal stealth constraint and carry out an automated design optimization of the S-duct. Moreover, traditional turbulence models have no enough mechanism of precisely

* Corresponding author.

E-mail address: ganhope@buaa.edu.cn (W. Gan).

predicting Reynolds stress and separation. It is difficult to obtain reliable analysis in optimization process. The numerical simulation method should be modified to improve accuracy of optimization design.

In this paper, a modified SST turbulent model is proposed and validated. Based on this model, an automated design system is constructed and used to obtain the optimal duct, whose on-design and off-design aerodynamic performances are particularly analyzed.

2. The numerical methods

2.1. The modified SST model

A k - ω shear stress transport model is proposed by Menter [10]. It combines the advantages of the original k - ε and k - ω models by using the k - ω model near the wall, and the k - ε model away from the wall. The transport equations of the model are summarized as follows:

$$\frac{\partial(\rho k)}{\partial t} + \rho u_j \frac{\partial k}{\partial x_j} = P_k \left(\frac{M_\infty}{Re} \right) - \beta' \rho k \omega \left(\frac{Re}{M_\infty} \right) + \frac{\partial}{\partial x_j} \left[\left(\mu + \frac{\mu_T}{\sigma_k} \right) \frac{\partial k}{\partial x_j} \right] \left(\frac{M_\infty}{Re} \right) \quad (1)$$

$$\frac{\partial(\rho \omega)}{\partial t} + \rho u_j \frac{\partial \omega}{\partial x_j} = P_\omega \left(\frac{M_\infty}{Re} \right) - \beta \rho \omega^2 \left(\frac{Re}{M_\infty} \right) + \frac{\partial}{\partial x_j} \left[\left(\mu + \frac{\mu_T}{\sigma_k} \right) \frac{\partial \omega}{\partial x_j} \right] \left(\frac{M_\infty}{Re} \right) + 2(1 - F_1) \frac{\rho}{\sigma_{\omega_2} \omega} \frac{\partial k}{\partial x_j} \frac{\partial \omega}{\partial x_j} \left(\frac{M_\infty}{Re} \right) \quad (2)$$

$$\mu_T = \min \left[\frac{\rho k}{\omega}, \frac{a_1 \rho k}{S F_2} \left(\frac{Re}{M_\infty} \right) \right] \quad (3)$$

where S is the magnitude of shear rate ($S = \sqrt{2S_{ij}S_{ij}}$). The production items are modeled as:

$$P_k = \mu_T S^2 \quad (4)$$

$$P_\omega = \frac{\gamma \rho P_k}{\mu_T} \quad (5)$$

The shear rate rapidly increases over the separation region and affects the accuracy of the Reynolds stress. Thus, the model is modified according to higher precise mechanism of predicting Reynolds stress (so-called based-Reynolds-stress idea [15]). Its production items and eddy viscosity are based on the magnitude of vorticity Ω ($\Omega = \sqrt{2\Omega_{ij}\Omega_{ij}}$) and are improved as follows:

$$P_k = \mu_T \Omega^2 - \frac{2}{3} \rho k \delta_{ij} \frac{\partial u_i}{\partial x_j} \quad (6)$$

$$\mu_T = \min \left[\frac{\rho k}{\omega}, \frac{a_1 \rho k}{\Omega F_2} \left(\frac{Re}{M_\infty} \right) \right] \quad (7)$$

The equilibrium assumption of transport equations is no longer suitable for separation [15]. The relationship between the production and dissipation of transport equations must be adjusted to increase the sensitivity of predicting separation. The model is modified with more mechanism of predicting separation (so-called based-separation idea [15]). It has a more suitable length scale and a more appropriate turbulent production mechanism over separation region. It can be summarized as five parts:

1) A blending function is constructed in Eq. (8) based on the production of turbulence kinetic energy,

Table 1

Mesh sizes for the grid convergence study.

Mesh	Total cells	Max y^+
Coarse	325 × 89	3.2
Medium	487 × 131	1.6
Fine	729 × 197	0.8
Extra-fine	1093 × 295	0.4

2) The constraint of the blending function is given in Eqs. (9) and (10),

3) The correction blending function of the length scale is employed in Eqs. (11) and (12),

4) The production of specific dissipation rate is improved in Eqs. (13) and (14),

5) The length scale and the turbulence production items are modified.

$$P_{rk\omega} = \frac{P_k}{\beta' \rho k \omega} \left(\frac{M_\infty}{Re} \right)^2 \quad (8)$$

$$f_1 = C_1 P_{rk\omega} - C_2 \quad (9)$$

$$f_2 = \min(\max(f_1, C_3), C_4) \quad (10)$$

$$r_d = \frac{\mu_T + \mu}{\rho U \kappa^2 d^2} \left(\frac{M_\infty}{Re} \right) \quad (11)$$

$$f_d = 1.0 - \tanh((8r_d)^3) \quad (12)$$

$$f_3 = f_2 f_d + (1.0 - f_d) \quad (13)$$

$$\overline{P_\omega} = f_3 P_\omega \quad (14)$$

where $U = \sqrt{(S_{ij}S_{ij} + \Omega_{ij}\Omega_{ij})/2}$, κ is Von Karman constant. $\overline{P_\omega}$ replaces P_ω in Eq. (2).

In addition to the model constants in Eqs. (12) and (13), the following constants are introduced in the model:

$$C_1 = 4, \quad C_2 = 5, \quad C_3 = 1, \quad C_4 = 12, \quad (15)$$

All constants are given to ensure the numerical simulation accuracy in many typical cases as Ref. [15].

2.2. The splitting method and boundary conditions

A structured Reynolds-averaged Navier-Stokes code is used as the flow solver [15]. The implicit approximate factor (AF) splitting time method [16] and Roe flux-difference splitting spatial discrete method are used. The turbulence transport equations have been solved with special handling. Their time discrete still uses AF method. Explicit processing is used for the production terms. The dissipation and diffusion terms are implicitly processed and employed as source terms. At solid boundaries, the no-slip condition enforces $k = 0$, ω satisfies $\omega = \frac{800\mu}{\rho d^2} \left(\frac{M_\infty}{Re} \right)^2$ as Ref. [10]. At far field boundaries, k is determined by freestream turbulence intensity, ω is specified as $\omega = k/0.009$ in Ref. [15].

2.3. Validations

The CFDVAL2004 includes a case without flow control [17]. To explain the modified mechanism step by step, the original, based-Reynolds-stress and full modified SST model are applied to predict separation for this case respectively. They are referred to as SST, SST-M1 and MSST. A family of grids is generated for which exact sizes are listed in Table 1. The computational domain extends $-1.95 \leq x/C_{re} \leq 3.64$ and $0 \leq y/C_{re} \leq 0.91$, where C_{re} is the distance from the onset of the hump to experiment reattachment point. At $x/C_{re} = -1.95$, the momentum-thickness Reynolds number is 6771 and the turbulence intensity is 0.5%.

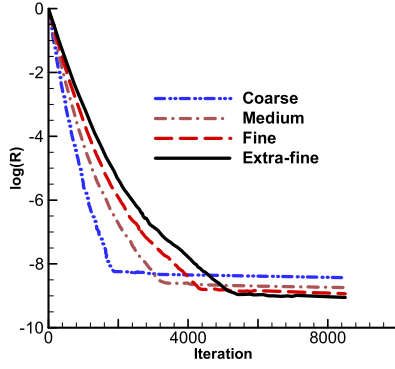


Fig. 1. Convergence of the density residual on the different meshes.

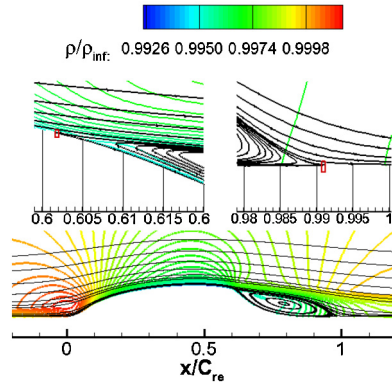


Fig. 2. The flow field for fine grid (MSST).

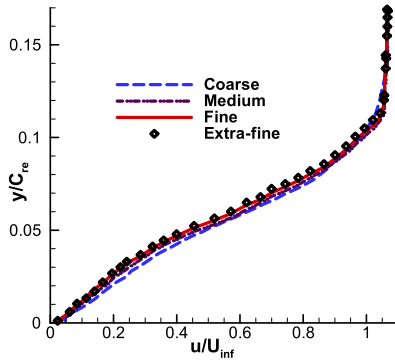


Fig. 3. Computational and experimental velocity profiles at $x/C_{re} = 1.00$.

Fig. 1 shows the density residual convergence of MSST for the four grids. The finer grids require more iterations to converge. Fig. 2 shows the computed flow field using MSST for the fine grid. It indicates the separation and reattachment points in the photomicrographs.

Fig. 3 represents typical velocity profiles using MSST ($x/C_{re} = 1.00$). Although the velocity profile predicted by the coarse mesh is different from others, the three finer grids have a similar feature of velocity profile.

In order to visualize the convergence behavior, the data points of separation and reattachment (determined by flow field, such as Fig. 2) are plotted in Fig. 4. A good level of convergence is achieved by three methods. The difference between the three finer meshes is less than 1% for both separation and reattachment.

Table 2 shows the comparison of fine grid computational and experimental results, which are nondimensionalized by reattachment distance. The difference between computational and experimental [18,19] result is small. The reattachment points of SST and

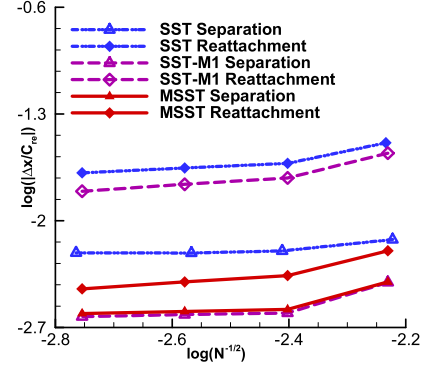


Fig. 4. Grid convergence of the aerodynamic coefficients. N is the total number of cells in the grid and $\Delta x/C_{re}$ is the difference between computation and experiment.

Table 2

The comparison of computation and experiment.

Location (x/x_{re})	SST	SST-M1	MSST	Exp
Separation	0.598	0.603	0.602	0.6045
Reattachment	0.975	1.024	0.991	1.000

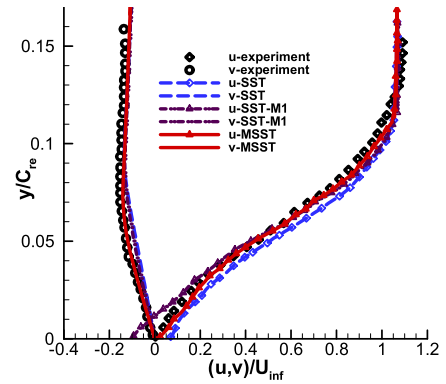


Fig. 5. Computational and experimental velocity profiles at $x/x_{re} = 1.00$.

SST-M1 are away from experiment. The result of MSST is in good agreement with experimental data.

Fig. 5 shows computational and experimental velocity profiles at $x/x_{re} = 1.00$. Velocity profiles of MSST are closer to experiment than SST and SST-M1. In fact, the SST model in previous publications [18,19] is always based on vorticity. The SST-M1 is similar with these publications, but has more precise production item of turbulent energy in Eq. (6). Thus, the reattachment point of the SST-M1 is away from the experimental result and a little similar with previous publications.

Fig. 6 represents computational and experimental [18] Reynolds stress. Compared with the experiment at $x/x_{re} = 1.00$, SST significantly overestimates Reynolds stress $\overline{u'v'}$, whereas SST-M1 underestimates Reynolds stress and is better than SST. MSST has better computational accuracy of Reynolds stress than SST-M1. At $x/x_{re} = 1.0909$, since it is away from reattachment point, computational results of various models tend to be consistent.

The rapidly increasing shear rate over the separation region can greatly cause the strengthen Reynolds stress $\overline{u'v'}$ of SST. Since the increase of vorticity is slower than shear rate over the separation region, SST-M1 has more reasonable turbulent production than SST. But it has low sensitivity of separation. Based on SST-M1, the separation-based modified SST turbulent model has good sensitivity of separation to improve the computational accuracy.

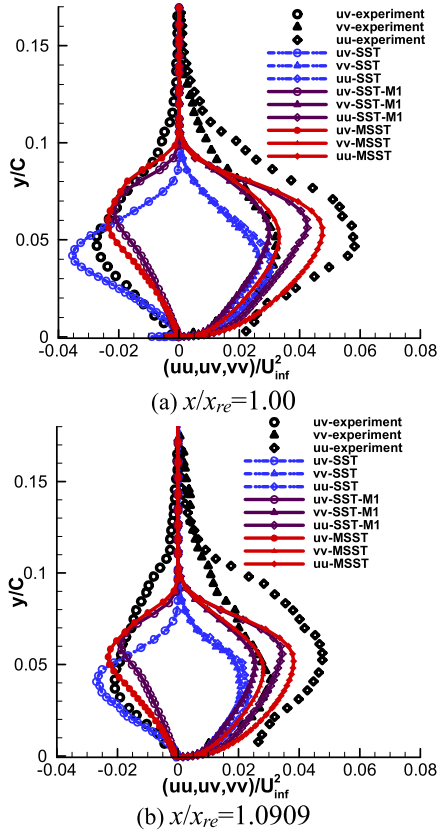


Fig. 6. Computational and experimental Reynolds stress.

Table 3
Mesh sizes of NASA S-duct.

Mesh	Total cells (O–H)	Max y^+
Coarse	$(29 \times 29 + 41 \times 113) \times 109$	3.6
Medium	$(57 \times 57 + 81 \times 225) \times 217$	0.9
Fine	$(113 \times 113 + 161 \times 449) \times 433$	0.225

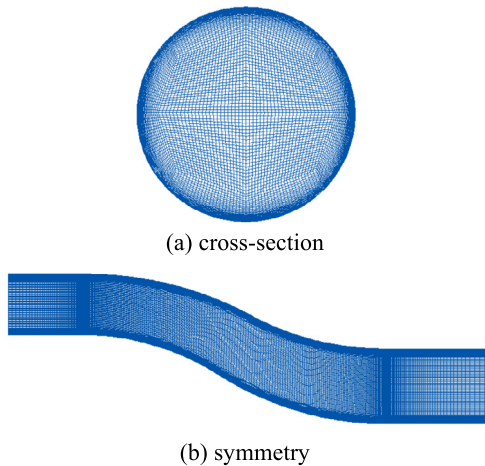


Fig. 7. The medium grid of NASA S-duct.

The experimental NASA S-duct was designed to study complex three-dimensional flow features, such as separation and secondary flows [20,21]. It is used for validated computation.

A family of grids is generated for which exact sizes are listed in Table 3. The grids are created by skipping every other point in

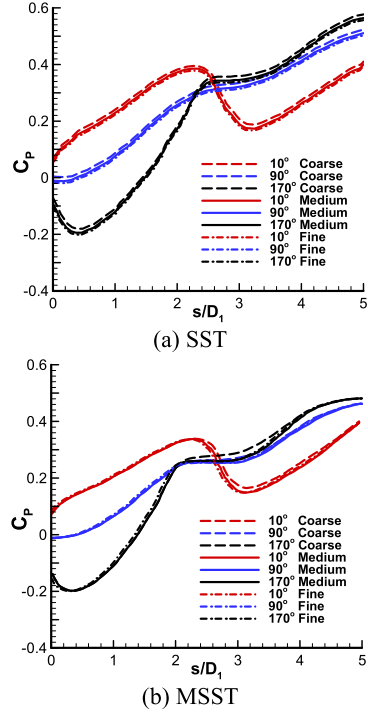


Fig. 8. Pressure coefficient for all grids.

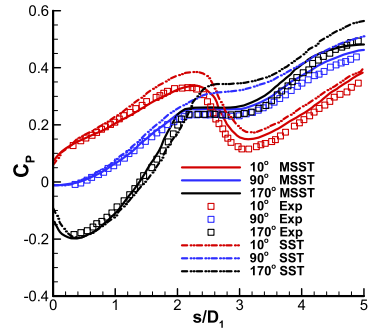


Fig. 9. Comparison of experimental and computed pressure coefficient based on the fine mesh.

the finer mesh. The first layer y^+ over the wall is increased four times.

The medium grid of the duct is shown in Fig. 7. The grid's density of symmetric plane is reasonable.

Fig. 8 shows pressure coefficient at 10°, 90° and 170° locations for all grids. Although the result of coarse method is different from the two fine grids, the pressure coefficient curves of two fine grids are almost superimposed for both SST and MSST.

A comparison of pressure coefficient along the duct's surface at 10°, 90° and 170° locations is shown in Fig. 9. The computations based on the fine mesh are compared with the experimental data [20]. The modified model suitability predicts the pressure coefficient along the duct's centerline for each angular location. It has better precision than SST model whose results are similar in Ref. [21].

The computed streamlines in the duct's symmetry plane, shown in Fig. 10, appear to be qualitatively very similar to those in experiment. But the highest point of the separation bubble in experiment is not obvious in computation.

Fig. 11 and Fig. 12 show the comparisons between the computational and experimental Mach number and the total pressure

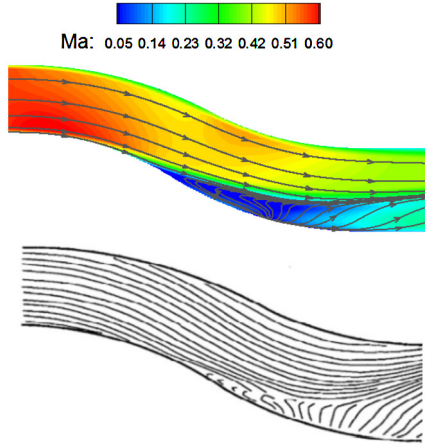


Fig. 10. Computed and experimental streamlines in the symmetry plane of the duct.

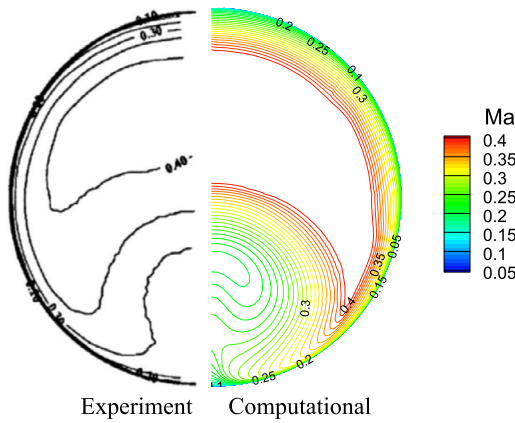


Fig. 11. Mach contours at aerodynamic interface plane (AIP).

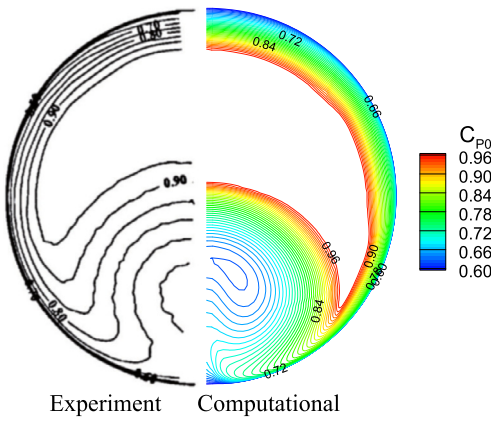


Fig. 12. The total pressure coefficient contours at AIP.

coefficient respectively at the aerodynamic interface plane (AIP). It is clear from Fig. 11 that the present model predicts the velocity distribution very well. The total pressure coefficient contours behave in a similar manner due to separation predicted in the computation, as seen in Fig. 12.

It is shown that the modified SST turbulent model is sufficiently robust and reliable to simulate aerodynamic features of VALCFD2004 and the typical S-duct. The model has almost equivalent computational cost as the original model and is fit for design and analysis of the S-duct.

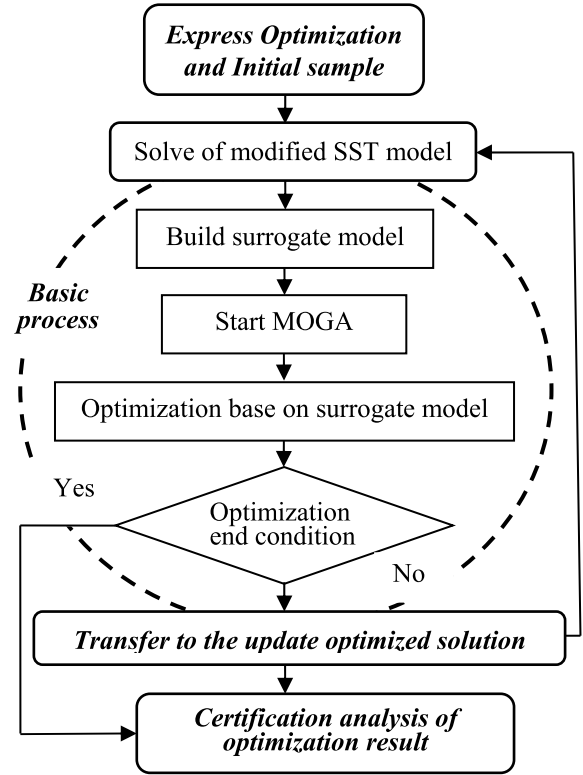


Fig. 13. The framework of the design system.

3. The automated design system

3.1. The framework of the design system

The design system combines with the modified SST turbulent model, radial basis function (RBF [22]) surrogate model and multi-object genetic algorithm. Fig. 13 shows the framework of the design system, which includes four parts. Firstly, taken into account conformal stealth constraint, the design problem is expressed as special parameter optimization problem. Secondly, the system builds RBF surrogate model and applies MOGA to optimization. Furthermore, some points of Pareto frontier are used as increased samples to carry out the updated optimization. Finally, the performance of the optimal result is analyzed and certified.

3.2. Experimental design and surrogate model

In the design process, the strategy of updated optimization selects partition Pareto solutions in each round of optimization operation. These solutions are solved by CFD and increased as sample points to improve the credibility of surrogate model. The Latin hypercube sample [23] is used as the initial experimental design. To enhance the efficiency of optimization, RBF is employed as the surrogate model. The RBF method is a feed forward neural network with strong self-adapt as Eq. (15) and is always used in aerodynamic optimization. Its details can be found in Ref. [15].

$$\hat{f}(x) = \sum_{k=1}^K \omega_k \phi(\|x - C_k\|) + b_k \quad (16)$$

3.3. Optimization algorithm and grid deformation

The multi-object genetic algorithm (MOGA [24]) is used to conduct the multi-object optimization. It has been real-coded as the

basic optimization algorithm. To evaluate the fitness of each individual in the population, the value of each objective is determined, and then the normalized value of fitness is expressed in Ref. [24]. The MOGA usually can handle complex aerodynamic optimization problems. The algorithm has four steps. At first, a random population in size N is generated. Secondly, after evaluation of initial population, non-dominated solutions are determined and archived. And then offspring population is generated using roulette wheel selection, crossover and mutation operators. At last, after producing child population, the next generation $(\lambda + \mu)$ -selection strategy is applied as survivor selection rule. In the process of survival selection, λ offspring are produced and calculated the respective fitness. And then, according to $(\lambda + \mu)$ -selection strategy, the best μ chromosomes in $\lambda + \mu$ ones are selected as the next population members in each generation [25]. In each generation, the archive of non-dominated solution is updated by the current population.

The transfinite interpolation (TFI [26]) method has been widely adapted to grid deformation. It is used to compute the displacements in the interior of the grid blocks. The displacement is computed by straight-line interpolation in the direction:

$$\begin{aligned} \vec{dx}^1(\xi, \eta, \varsigma) = & \omega_1(\xi, \eta, \varsigma)(1 - t_{\xi, \eta, \varsigma})\vec{dx}(0, \eta, \varsigma) \\ & + \omega_2(\xi, \eta, \varsigma)t_{\xi, \eta, \varsigma}\vec{dx}(NI, \eta, \varsigma) \end{aligned} \quad (17)$$

Then the mismatch of the displacements must be added along the other two directions.

$$\begin{aligned} \vec{dx}^2(\xi, \eta, \varsigma) = & \vec{dx}^1(\xi, \eta, \varsigma) + \omega_3(\xi, \eta, \varsigma)(1 - s_{\xi, \eta, \varsigma})(\vec{dx}(\xi, 0, \varsigma) \\ & - \vec{dx}^1(\xi, 0, \varsigma)) + \omega_4(\xi, \eta, \varsigma)s_{\xi, \eta, \varsigma}(\vec{dx}(\xi, NJ, \varsigma) \\ & - \vec{dx}^1(\xi, NJ, \varsigma)) \end{aligned} \quad (18)$$

$$\begin{aligned} \vec{dx}^3(\xi, \eta, \varsigma) = & \vec{dx}^2(\xi, \eta, \varsigma) + \omega_5(\xi, \eta, \varsigma)(1 - u_{\xi, \eta, \varsigma})(\vec{dx}(\xi, \eta, 0) \\ & - \vec{dx}^2(\xi, \eta, 0)) + \omega_6(\xi, \eta, \varsigma)u_{\xi, \eta, \varsigma}(\vec{dx}(\xi, \eta, NK) \\ & - \vec{dx}^2(\xi, \eta, NK)) \end{aligned} \quad (19)$$

Finally, the grid deformation is finished as

$$\vec{dx}(\xi, \eta, \varsigma) = \vec{dx}^3(\xi, \eta, \varsigma) \quad (20)$$

4. The design optimization and analysis

4.1. The design problem

In the design process, based on conformal stealth constraint of the aircraft, the airframe's shape and the duct's inlet station are firstly determined to meet requirement of stealth. Fig. 14 shows the shape schematic of the duct and airframe. The shape of the duct is parameterized. The solid model and grid are automatically updated using the TFI method. The design process includes several CFD computations, reconstructions of surrogate model, iterates of optimization.

Fig. 15 is multi-directional view of the duct, which is based on conformal stealth constraint. The centerline, area ratio and off-set are parameterized, and respectively described as Eq. (21), (22) and (23).

$$y - y_0 = [a_1(\Delta x)^2 + b_1(\Delta x)^3 + c_1(\Delta x)^4 + d_1(\Delta x)^5] + x_0 \quad (21)$$

$$\frac{A}{A_1} = \left(\frac{A_2}{A_1} - 1 \right) [a_2(\Delta x)^2 + b_2(\Delta x)^3 + c_2(\Delta x)^4] + 1 \quad (22)$$

$$z - z_0 = [a_3(\Delta x) + b_3(\Delta x)^2 + c_3(\Delta x)^3] + x_0 \quad (23)$$

Fig. 16 shows the surface mesh of the S-duct. The grid's density is reasonable.

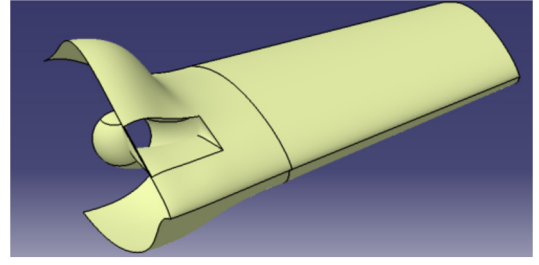


Fig. 14. The shape of the S-duct and fuselage.

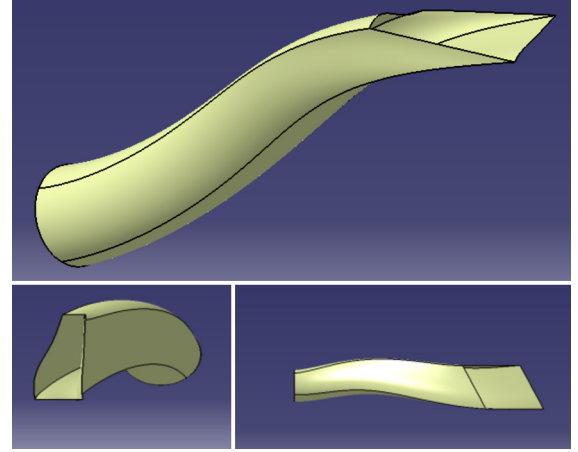


Fig. 15. The multi-directional view of the S-duct.

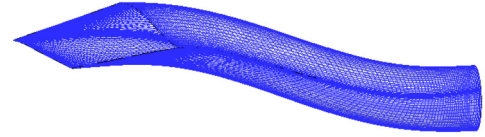


Fig. 16. The surface mesh of the S-duct.

4.2. Design results and analysis

The design goals are the total pressure recovery σ_{P_0} and the total pressure distortion DC_{60} at design state (Eq. (24) and Eq. (25)). The design state is $Ma = 0.6$, $\alpha = 2^\circ$.

$$\sigma_{P_0} = \frac{\overline{P_{0, outlet}}}{\overline{P_{0, inlet}}} \quad (24)$$

$$DC_\psi = \max_{0 \leq \phi \leq 2} \frac{[\overline{P_0} - \overline{P_0}(\phi, \psi)]}{\bar{q}} \quad (25)$$

where \bar{q} is the mean dynamic pressure with $\bar{q} = \frac{1}{2}\rho V^2$, ρ is the density and V is the magnitude of the velocity, and $\overline{P_0}$ is the mean total pressure.

$$\overline{P_0} = \frac{\int_0^{2\pi} \int_0^R P_0(r, \theta) r dr d\theta}{\int_0^{2\pi} \int_0^R r dr d\theta} \quad (26)$$

$$\overline{P_0}(\phi, \psi) = \frac{\int_0^\psi \int_0^R P_0(r, \phi + \theta) r dr d\theta}{\int_0^\psi \int_0^R r dr d\theta} \quad (27)$$

$$\bar{q} = \frac{\int_0^{2\pi} \int_0^R \frac{1}{2} \rho V^2 r dr d\theta}{\int_0^{2\pi} \int_0^R r dr d\theta} \quad (28)$$

The angle ϕ is the starting angle of a pie-shaped slice of angle ψ over which the total pressure is integrated. When ψ is 60° in Eq. (27), the coefficient DC_{60} has been defined.

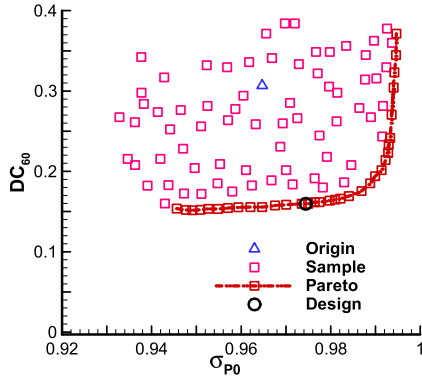


Fig. 17. Samples and Pareto frontier.

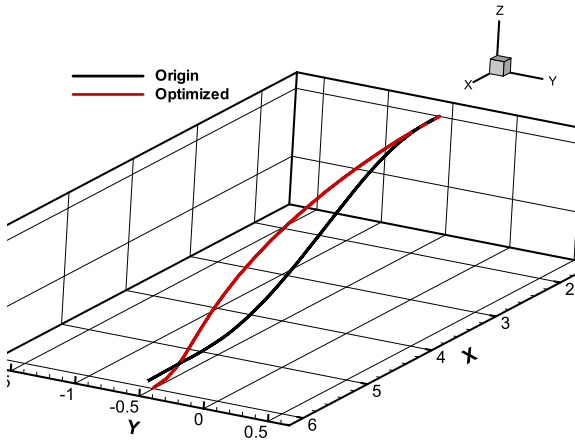


Fig. 18. The centerlines of S-ducts.

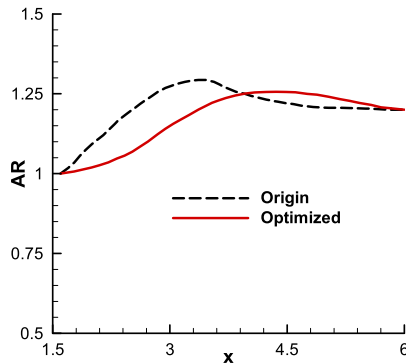


Fig. 19. Area ratio vs. distance.

Fig. 17 shows results of Pareto frontier in the last updated optimization and all sample points. The distribution of Pareto frontier is uniform. In the optimization process, Latin hypercube sample has got 61 sample points. There are 5 increased sample points, which are always near the Pareto frontier, in each updated optimization. The total of 15 sample points are added to construct update RBF. Four rounds of updated optimization converge to global minimal. Therefore, 76 design shapes are carried out CFD calculations in all. There are 18 times verified calculation for design result. It is shown that the design optimization has low computation cost and excellent optimization efficiency.

The centerlines of original and optimization design are given in Fig. 18. Obviously, compared to the original design, the centerline of the optimal duct is smoother and has more suitable offset. It helps to reduce the flow distortion and the total pressure loss.

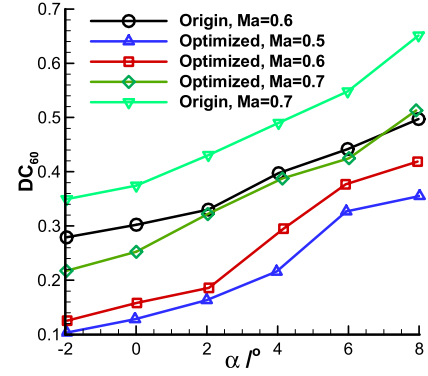


Fig. 20. The distortion coefficient at different Mach.

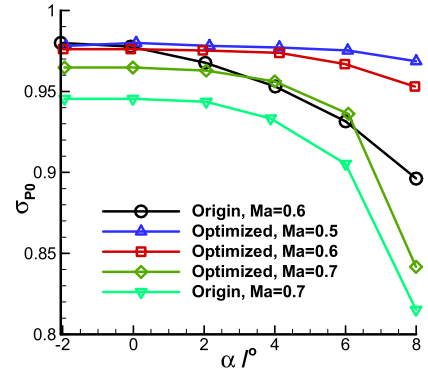


Fig. 21. The total pressure recovery factor at different Mach.

Fig. 19 is the comparison of the cross-sectional area ratio. The optimal duct has smaller area ratio than the original duct in the front half. The centerline's curvature and the area ratio of the optimal duct are reasonable to avoid overexpand.

The distortion coefficient of the optimal S-duct is reduced by 16.3%, and the total pressure recovery factor is increased by 1.1% at design state (as shown in Fig. 20 and Fig. 21). As Mach and attack angle increase, the total pressure recovery is smaller and the distortion coefficient becomes larger.

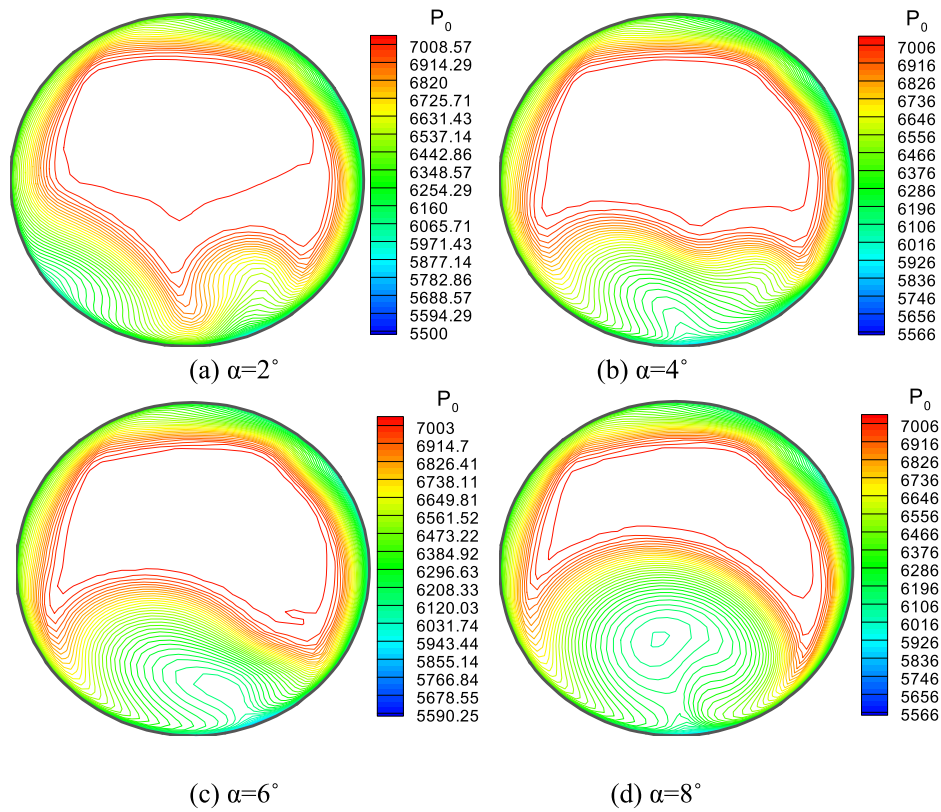
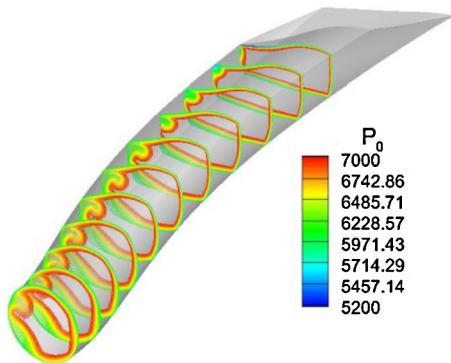
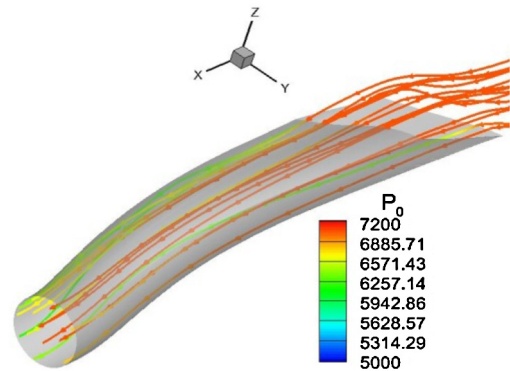
Fig. 22 represents total pressure distributions of the outlet at $Ma = 0.6$. There are two distortion regions of low total pressure at $\alpha = 2^\circ$. But they mix into one at $\alpha \geq 4^\circ$. With attack angle increasing, low total pressure region and separation region gradually extend, but adverse pressure gradient of boundary layer enhances.

Fig. 23 shows total pressure distributions at $Ma = 0.6$, $\alpha = 2^\circ$. The edges of the inlet are conformal with the airframe. They induce inhomogeneous flow to cause flow distortion. The distortion increases along the streamwise. The secondary flow and two low total pressure regions appear at rear. Fig. 24 illustrates streamlines at $Ma = 0.6$, $\alpha = 2^\circ$. Obviously, there are cross flow characteristics at the rear of the duct.

Fig. 25 represents turbulent vortices at $\alpha = 2^\circ$ and $\alpha = 8^\circ$ ($Ma = 0.6$). The vortices gradually increase and concentrate into the inhomogeneous total pressure region. And then, they rapidly concentrate into the secondary flow region. There are a significant high vortex region and a vortex core at $\alpha = 8^\circ$.

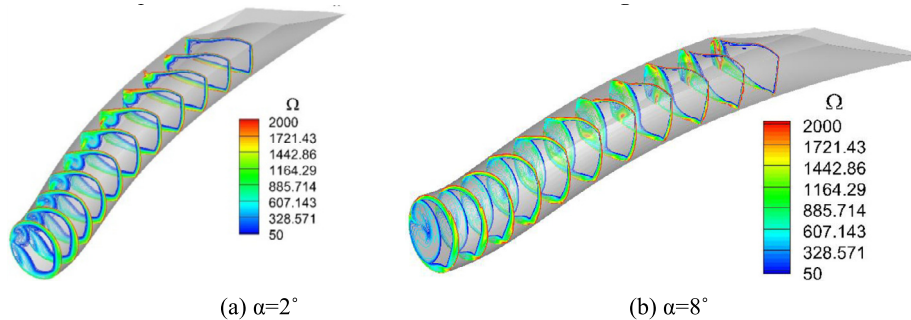
Fig. 26 shows total pressure distributions of the outlet at $Ma = 0.5$ and 0.7 . The flow characteristics of $Ma = 0.5$ and 0.6 have certain similarities (as Fig. 22). But the flow features of $Ma = 0.7$ are special. There is a large region of low total pressure at $Ma = 0.7$, $\alpha = 6^\circ$. The low total pressure region changes into a large recirculation region at $Ma = 0.7$, $\alpha = 8^\circ$.

Fig. 27 illustrates total pressure distributions of different Mach at $\alpha = 8^\circ$. The distortion of total pressure is small at $Ma = 0.5$,

Fig. 22. Total pressure distributions of the outlet at $Ma = 0.6$.Fig. 23. Total pressure distributions of $Ma = 0.6$, $\alpha = 2^\circ$.Fig. 24. Streamlines of $Ma = 0.6$, $\alpha = 2^\circ$.

but is very large at $Ma = 0.7$. In fact, since freestream velocity increases, there are wave shocks of outflow. They lead to strong adverse pressure, shock/boundary layer interaction and large separation. These could enhance flow distortion of the duct.

Fig. 28 shows turbulent vortices of different Mach at $\alpha = 8^\circ$. At $Ma = 0.5$, the variation of vortices corresponds with total pressure distribution (Fig. 27a). At the secondary flow region, vortices

Fig. 25. Turbulent vortices at different attack angles ($Ma = 0.6$).

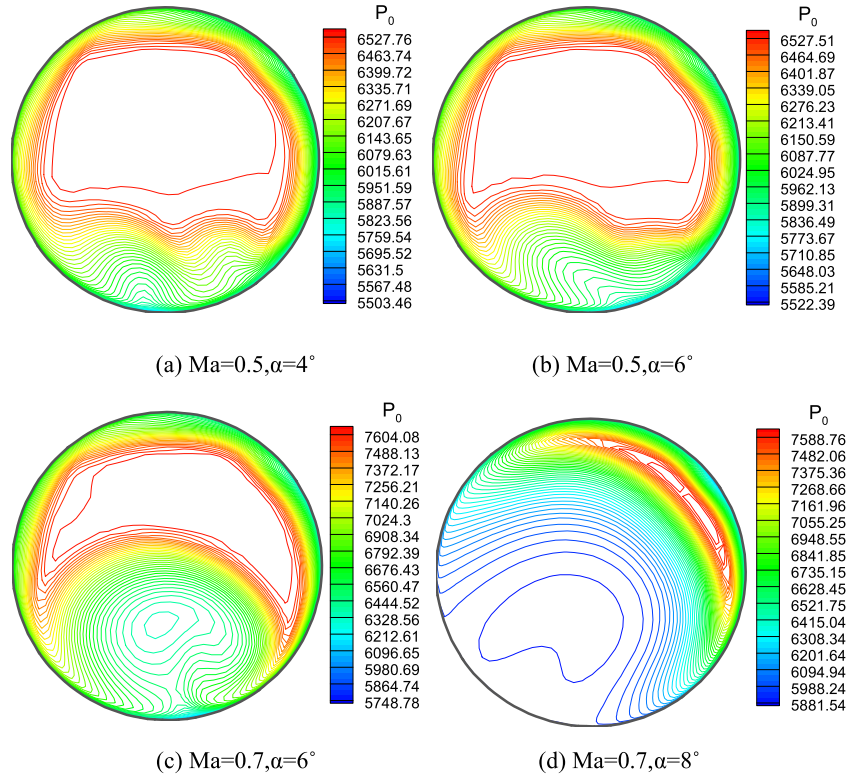


Fig. 26. Total pressure distributions of the outlet at $Ma = 0.5$ and $Ma = 0.7$.

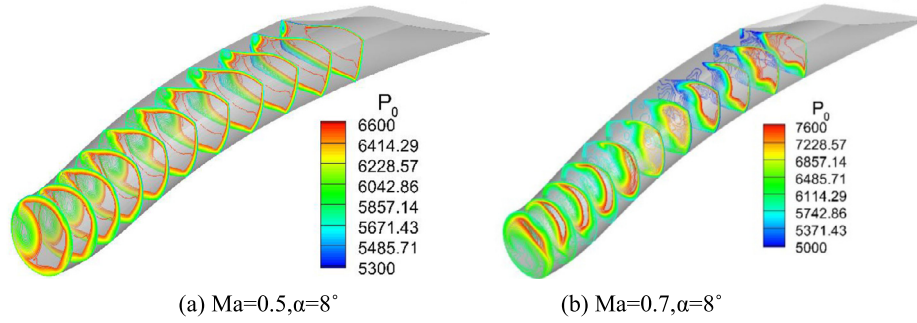


Fig. 27. Total pressure distributions of different Mach at $\alpha = 8^\circ$.

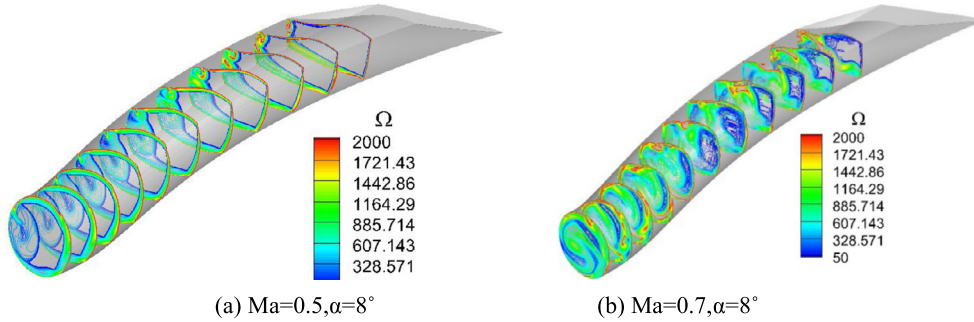


Fig. 28. Turbulent vortices of different Mach at $\alpha = 8^\circ$.

change obviously. Compared to $Ma = 0.5$ and $Ma = 0.6$ (Fig. 25b), there are flow features of larger distortion at $Ma = 0.7$.

Taken together, aerodynamic performance of $Ma = 0.5$ is as good as on-design condition ($Ma = 0.6$), but the performance of $Ma = 0.7$ rapidly decreases just like with the original S-duct.

5. Conclusions

A modified Menter's $k-\omega$ SST turbulent model is proposed by based-Reynolds-stress and based-separation ideas. Validation of the model including grid convergence has been performed and

shows that the present implementation is sufficiently robust and suitable to use in aerodynamic design of the S-duct.

Based on the modified SST model, an automated design system is set up and used to gain an optimal S-duct. The system can take into account conformal stealth constraint and well combine with the present turbulent model, RBF surrogate model and multi-object genetic algorithm. It has low computation cost and excellent design efficiency.

The optimal S-duct has suitable parameters of the centerline and the cross-sectional area ratio to avoid overexpand. Compared with original design, its flow distortion coefficient is reduced by 16.3% and total pressure recovery factor is increased by 1.1% in design condition. Its low-speed off-design performance is as good as on-design, but high-speed performance is decreased.

Conflict of interest statement

None declared.

References

- [1] J.R. Weske, Pressure loss in ducts with compound elbows, NACA Wartime Rept. W-39, National Advisory Committee for Aeronautics, 1943.
- [2] R. Guo, J. Seddon, An investigation of swirl in an S-duct, *Aeronaut. Q.* 33 (1982) 25–58.
- [3] J. Seddon, E. Goldsmith, Intake Aerodynamics, American Institute of Aeronautics and Astronautics, Reston, VA, 1985.
- [4] E. Goldsmith, J. Seddon, Practical Intake Aerodynamic Design, Blackwell Scientific Publications, Boston, 1993.
- [5] Q. Xiao, M.H. Tsai, Computation of transonic diffuser flows by a lagged $k-\omega$ turbulence model, *J. Propuls. Power* 19 (2003) 473–483.
- [6] K. Saha, S.N. Singh, V. Seshadri, Computational analysis on flow through transition S-diffusers: effect of inlet shape, *J. Aircr.* 44 (2007) 187–193.
- [7] G.A. Gerolymos, S. Joly, M. Malle, I. Vallet, Reynolds-stress model flow prediction in aircraft-engine intake double-S-shaped duct, *J. Aircr.* 47 (2010) 1368–1381.
- [8] W. Zhang, D. Knight, D. Smith, Automated design of subsonic diffuser, *J. Propuls. Power* 16 (2000) 1132–1140.
- [9] B.J. Lee, C. Kim, Automated design methodology of turbulent internal flow using discrete adjoint formulation, *Aerosp. Sci. Technol.* 11 (2007) 163–173.
- [10] F.R. Menter, Two-equation eddy-viscosity turbulence models for engineering applications, *AIAA J.* 32 (1994) 1598–1605.
- [11] J.M. Zhang, C.F. Wang, K.Y. Lum, Multidisciplinary design of S-shaped intake, *AIAA Paper* 2008-7060, 2008.
- [12] A. Aranake, J.G. Lee, D. Knight, R.M. Cummings, J. Cox, M. Paul, A.R. Byerley, Automated design optimization of a three-dimensional subsonic diffuser, *J. Propuls. Power* 27 (2011) 838–846.
- [13] T. Magnus, Design and analysis of compact UAV ducts, *AIAA Paper* 2006-2828, 2006.
- [14] A.R. Paul, P. Ranjan, V.K. Patel, A. Jain, Comparative studies on flow control in rectangular S-duct diffuser using submerged-vortex generators, *Aerosp. Sci. Technol.* 28 (2013) 332–343.
- [15] W.-B. Gan, Research on aerodynamic numerical simulation and design of near space low-Reynolds-number unmanned aerial vehicles, Ph.D. Dissertation, Northwestern Polytechnical University, Xi'an, 2014.
- [16] S.L. Krist, R.T. Biedron, C.L. Rumsey, CFL3D user's manual: ver. 5.0, NASA NASA-TM/1998-208444, 1998.
- [17] C.L. Rumsey, T.B. Gatski, W. Sellers, N. Vatsa, S. Viken, Summary of the 2004 computational fluid dynamics validation workshop on synthetic jets, *AIAA J.* 44 (2006) 194–207.
- [18] C.L. Rumsey, Proceedings of the 2004 workshop on CFD validation of synthetic jets and turbulent separation control, NASA/CP-2007-214874, 2007.
- [19] A. Avdis, S. Lardeau, M. Leschziner, Large eddy simulation of separated flow over a two-dimensional hump with and without control by means of a synthetic slot-jet, *Flow Turbul. Combust.* 83 (2009) 343–370.
- [20] S.R. Wellborn, T.H. Okiishi, B.A. Reichert, A Study of Compressible Flow Through a Diffusing S-Duct, NASA-TM/1993-106411, 1993.
- [21] C. Fiola, R.K. Agarwa, Simulation of secondary and separated flow in a diffusing S-duct using four different turbulence models, *Proc. Inst. Mech. Eng., Part G, J. Aerosp. Eng.* 28 (2014) 1954–1963.
- [22] I.R.H. Jackson, Convergence properties of radial basis function, *Constr. Approx.* 4 (1988) 243–246.
- [23] J. Sacks, W.J. Welch, T.J. Michel, H.P. Wynn, Design and analysis of computer experiments, *Stat. Sci.* 4 (1989) 409–435.
- [24] E. Zitzler, L. Thiele, Multi-objective evolutionary algorithms: a comparative case study and the strength Pareto approach, *IEEE Trans. Evol. Comput.* 3 (1999) 257–271.
- [25] G. Zhou, H. Min, M. Gen, A genetic algorithm approach to the bi criteria allocation of customers to warehouses, *Int. J. Prod. Econ.* 86 (2003) 35–45.
- [26] R.E. Smith, Transfinite Interpolation (TFI) Generation Systems, CRC Press Inc., London, 1999.